Structural analysis of tilvestamab in complex with AXL

Eleni Christakou [1,2], Andrea J. Lopez [1], Gopinath Muruganandam [3,4], David Micklem [2], James B. Lorens [1,5], Petri Kursula [1,6,*]

[1] Department of Biomedicine, University of Bergen, Norway

[2] BerGenBio ASA, Bergen, Norway.

[3] VIB-VUB Center for Structural Biology, Vlaams Instituut voor Biotechnologie, Brussels, Belgium

[4] Structural Biology Brussels, Department of Bioengineering Sciences, Vrije Universiteit Brussel (VUB), Brussels, Belgium

[5] Centre for Cancer Biomarkers, Norwegian Centre of Excellence, University of Bergen, Bergen, Norway.

[6] Faculty of Biochemistry and Molecular Medicine, University of Oulu, Finland

*address for correspondence: petri.kursula@uib.no

Abstract

AXL is a receptor tyrosine kinase with a significant role in various biological processes and important medical implications, particularly in cancer. AXL transduces signals from the extracellular environment into the cytoplasm by binding to its ligand, growth arrest-specific protein 6 (GAS6). Activation of AXL leads to autophosphorylation of its intracellular domain and subsequent activation of downstream signaling pathways involved in cell proliferation, migration, differentiation, and survival. Tilvestamab (also known as BGB149) is a first-in-class, humanized, therapeutic anti-AXL function-blocking monoclonal antibody. We carried out a structural characterization of the AXL-tilvestamab complex, using both negative-stain and cryogenic transmission electron microscopy as well as synchrotron small-angle X-ray scattering. While AXL-Fc was highly elongated and formed large, heterogeneous complexes with the full antibody, homogeneous samples for structural studies could be made using the monomeric soluble AXL extracellular domain, the Fab fragment of tilvestamab, and an anti-Fab nanobody. Both SAXS and cryo-EM confirmed successful complex formation between the three proteins, and a low-resolution 3D model for the tilvestamab-AXL complex is presented. The data allow for sample optimization for high-resolution structural biology as well as designing mutations that could alter binding affinity and specificity.

Introduction

AXL is a member of the TAM (TYRO3, AXL, MERTK) family of receptor tyrosine kinases (RTKs), which play critical roles in maintaining tissue homeostasis and regulation of the innate immune system[1,2]. In a disease setting, AXL signaling is associated with aggressive, drug-resistant, and immune-resistant tumor phenotypes[3,4], fibrosis[5] and may facilitate infection with a range of viruses[6].

AXL is comprised of an extracellular ligand-binding domain with two immunoglobulin-like (Ig) and two fibronectin type III domains, a single transmembrane helix, and an intracellular tyrosine kinase domain[7]. AXL is activated by the growth arrest-specific protein 6 (GAS6)[8-10], leading to activation of multiple downstream pathways depending on the cell type and context [11]. The AXL Ig1 and Ig2 domains are important for GAS6 binding and thereby receptor activation. Earlier structural studies have provided insights into the AXL-GAS6 interactions necessary for activation[12].

Due to its involvement in human disease, AXL has gained strong interest towards therapeutic and diagnostic applications, in addition to its importance to fundamental biology. In oncology, AXL overexpression is linked to poor prognosis, metastasis, and resistance to conventional treatments[13-16]. Consequently, AXL is considered a promising therapeutic target, with both small-molecule inhibitors[17-19] and monoclonal antibodies [20] under development aimed at blocking its function. AXL is additionally implicated in fibrotic diseases and immune disorders, and it could function in internalization of viral particles, including SARS-CoV-2[21], broadening the scope of its therapeutic and diagnostic potential.

Tilvestamab (BGB149) is a fully humanized monoclonal function-blocking anti-AXL therapeutic antibody, developed by BerGenBio. The tilvestamab-AXL interaction blocks the GAS6-mediated AXL activation, thereby inhibiting the receptor´s downstream signaling pathways involved in disease progression[20,22,23]. Details on the antibody-antigen complex at the molecular level would be of great benefit to further develop this tool and understand molecular mechanisms of disease and possible treatments.

We aimed at a structural characterisation of the complex between tilvestamab and AXL. Using both experimental negative-stain transmission electron microscopy (TEM), small-angle X-ray scattering (SAXS), and cryogenic electron microscopy (cryo-EM), as well as AlphaFold3 modelling[24], we build a model for the AXL-tilvestamab complex

that can further be used to understand binding determinants in the complex, the molecular mechanisms of functional inhibition, and the inherent flexibility of the AXL extracellular domain. Our findings provide a foundation for high-resolution experimental structure determination of the AXL-tilvestamab complex, with potential applications in treatment and diagnosis of AXL-related diseases.

Materials and methods

Preparation of protein samples

Human AXL-Fc containing the entire extracellular domain of human AXL was purchased from Evitria (Switzerland). Monomeric sAXL, comprising the soluble extracellular domain of AXL, was prepared by papain digestion, followed by protein A purification, as previously described[25].

Tilvestamab (BGB149, BerGenBio, Norway), a humanized AXL monoclonal antibody [20] was obtained from BerGenBio. The Fab fragment of tilvestamab was prepared by papain proteolysis and purified using standard protocols. Briefly, 3 ml (60 mg) tilvestamab were dialysed against PBS overnight. Digestion buffer was prepared just before use (PBS + 20 mM cysteine HCl + 20 mM EDTA, pH 7). 1.5 ml of 50% immobilized papain slurry (Thermo Scientific, 20341) was pipetted to a 15 ml falcon tube using a cut pipette tip, and 12 ml of digestion buffer were added to the gel slurry. After centrifugation (300 rpm RT), washing was repeated, and washes were discarded both times. The gel was resuspended in 1.5 ml digestion buffer (1:1). 3 ml of dialysed tilvestamab were added, and the sample was shaken at 37 °C for 2.5 h. After digestion, the sample was centrifuged (3000 rpm, 4 °C) and supernatant was recovered. Another elution was done with 0.5 ml PBS. Supernatants were spun down and filtered through a 0.45-µm filter, before applying to the MabSelect SuRe column. The eluate from the column was analysed by SDS-PAGE.

The anti-NabFab nanobody[26] cDNA was cloned into the pTH27 vector[27] and expressed in *E. coli* BL21 Rosetta cells. Cells were grown in 0.8 L LB media supplemented with 100 µg/ml of ampicillin and 34 µg/ml of chloramphenicol at 37 ºC until an OD of 0.5 was reached. Then, 1 mM IPTG was added, and the cells were grown for 20 h at 20 °C. Harvested pellets were resuspended with 20 mM Hepes, pH 7.5, 0.1 mg/ml of lysozyme, 0.5 mM TCEP, 10 mM Imidazole, and the cOmplete™, EDTA-free Protease Inhibitor Cocktail (Merck). The cell suspension was lysed by sonication and centrifuged at 20 000 g for 15 min at 4 °C. The supernatant was filtered through a 0.45 mm membrane (Sarstedt REF 831826) and loaded into a 3 ml of Ni-NTA agarose column, pre-equilibrated with equilibration buffer (20 mM Hepes pH 7.5, 250 mM NaCl, 0.5 mM TCEP) with 10 mM imidazole. The column was washed 4 CV with equilibration buffer with 10 mM imidazole and 8CV with 20 mM imidazole. The last wash of 9 CV with 20 mM Hepes pH 7.5, 100 mM NaCl, and 20 mM imidazole.

113 The protein was eluted with 20 mM Hepes pH 7.5, 100 mM NaCl, and 350 mM
114 Imidazole. The His-tag was cleaved with tobacco etch virus (TEV) protease during
115 dialysis for 16 h in 20 mM Hepes 7.5 pH, 100 mM NaCl, and 1 mM DTT followed by
116 reverse Ni-NTA chromatography. The eluted protein was gel filtered with Hiload 16/600
117 Superdex 75 column pre-equilibrated with 20 mM Hepes pH 7.5, 100 mM NaCl, and
118 0.5 mM TCEP. The quality of the purified protein was analyzed by sodium dodecyl
119 sulfate polyacrylamide gel electrophoresis (SDS-PAGE).

120

121 ***Negative stain electron microscopy***

122 Prior to sample application, formvar/carbon grids with copper mesh (Electron
123 Microscopy Sciences) were glow-discharged in an ELMO glow discharge unit for 30
124 s. Samples were diluted 1:10, 1:100 and 1:1000 for initial screening. For negative
125 staining, a 2 µl drop of sample solution was absorbed to a freshly glow-discharged
126 grid, washed with three drops of deionized water and stained with three drops of
127 freshly prepared 1% uranyl formate. Micrographs were recorded at room temperature
128 on a JEM-1400 electron microscope (JEOL) equipped with a LaB6 cathode and
129 operated at 120 kV. Images were acquired with a 4096 × 4096 pixel CMOS TemCam-
130 F416 camera (TVIPS) at a nominal magnification of 60000 and a corresponding pixel
131 size of 2.29 Å under a defocus between 2.5 and 5.0 µm.

132

133 ***Small-angle X-ray scattering in solution***

134 Small-angle X-ray scattering (SAXS) data from AXL, tilvestamab, Fabs of tilvestamab
135 and complexes of AXL and tilvestamab were collected on the SWING beamline of
136 Soleil synchrotron (Saint Aubin, France) in HPLC mode [28]. The data were collected
137 using a wavelength (λ) of 1.033 Å and a sample-to-detector (EIGER X 4M) distance
138 of 2.0 m, resulting in a momentum transfer (q) range of 0.004-0.5 $Å^{-1}$ ($q = 4\pi \sin \theta \lambda^{-1}$;
139 where 2θ is the scattering angle). This setup enabes samples to pass first through a
140 SEC column and later into a capillary where they are exposed to X-rays and allows
141 the collection of hundreds of scattering curves from the SEC peak that corresponds to
142 the sample of interest. Prior to SEC-SAXS analysis, samples were centrifuged at
143 20798 g for 10 min at 4 °C. For each measurement, 50 µl of the sample was injected
144 onto a BioSEC-3 300 or BioSEC-5 1000 column (Agilent Technologies) pre-
145 equilibrated with PBS or 10 mM histidine, 150 mM NaCl, pH 6. The flow rate was 0.3

146 ml/min. SAXS data were recorded with an exposure time of 990 ms per frame and a
147 dead time of 10 ms between frames. Buffer data were collected at the beginning of the
148 chromatogram. Data reduction, R_g evaluation over elution profiles, data averaging,
149 and merging were performed using the beamline software Foxtrot (version 3.5.2).
150 Subsequent final data processing and model building were carried out using the
151 ATSAS package[29], with CHROMIXS being used to obtain scattering curves for SEC-
152 SAXS data[30]. Distance distributions were obtained using GNOM[31], and *ab initio*
153 models were built with DAMMIN [32] for dummy atom-based modelling, and MONSA for
154 a comprehensive multi-phase modelling[29]. During the project, test data were also
155 collected on the CoSAXS beamline at MAX-IV synchrotron (Lund, Sweden)[33], but the
156 data presented here are from SOLEIL, as they were all collected using the same
157 beamline and settings.

158

159 ***Cryo-EM sample preparation and data collection***

160 0.25 mg of sAXL was mixed with Fab fragments from tilvestamab and the anti-NabFab
161 nanobody in a 1:2:3 molar ratio. The sample was incubated on ice for 30 min and
162 subjected to SEC using a Supersex 200 increase 10/300 column. Cryo-EM grids of
163 the complex at 0.33 mg/ml were prepared by applying 3 µl to airglow discharged 300
164 mesh copper C-flat R1.2/1.3 or Au-flat R 0.6/1 grids, which were then plunged into
165 liquid ethane using a Vitrobot (FEI Mark IV).

166 18747 movies were collected at the iNANO centre (Aarhus University, Denmark) using
167 a Titan Krios electron microscope (FEI) operated at 300 kV with a K3 Summit direct
168 electron detector (Gatan) with GIF Energy Filter. Each movie was dose-fractionated to
169 53 frames with a dose rate of 1.2 $e^-/Å^2$/frame for a total dose of 59.6 to 60.5 $e^-/Å$. The
170 total exposure time was 1.4 s.

171

172 **Image Processing**

173 The collected data was processed using cryoSPARC v.3.1.0[34]. Particle picking was
174 performed with the Blob Picker job, and particles were extracted with a box size of 280
175 pixels. These particles were subjected to 2D classification, with a batch size of 1,000
176 particles per class and 60 online-EM iterations. The resulting 2D classes were used
177 as templates for subsequent particle picking, where the box size was increased to 480
178 pixels. A second round of 2D classification was performed, and the selected 2D

classes were used to generate an initial 3D model via *ab initio* reconstruction, with an initial and final minibatch size of 300 and 1000 particles, respectively. The *ab initio* reconstruction consisted of five classes and was followed by heterogeneous and non-uniform refinement to improve particle alignment and map resolution. Local refinement was performed using the best 3D class to enhance the map of the additional density that is suspected to correspond to the binding region of the Ig domain.

Model Building and Refinement

The atomic model of the tilvestamab Fab and the antiNabFab nanobody was constructed based on the cryo-EM structure 7pij[26]. The models of NabFab and the antiNabFab nanobody were fitted into the cryo-EM map using ChimeraX v.1.8[35]. The tilvestamab Fab sequence was then used to mutate the model in Coot v.9.8.93[36]. Namdinator[37] was used to fit the initial atomic model to the density map and correct the model geometry. Subsequent refinement steps were performed iteratively in reciprocal space using Phenix v.1.19.2[38]. Finally, the AXL Ig1 domain was modeled using AlphaFold3 and fitted into the extra density using ChimeraX v.1.8.

Data availability

All data are available online through Zenodo.org or dedicated databases (EMDB, PDB, SASDB). Access codes and DOIs will be updated here.

Results and discussion

Imaging of tilvestamab and AXL using electron microscopy

Already from previous work, we knew that the dimeric AXL-Fc and monomeric sAXL are elongated and flexible[25]. For a first characterisation of AXL and tilvestamab samples for structural studies, we carried out negative stain EM imaging of the proteins alone and in complex. The antibody alone showed both monomeric and dimeric particles, while in complex with AXL-Fc, heterogeneous large particles were observed. While the latter confirmed complex formation, it also indicated high conformational flexibility and the formation of larger-order oligomers. This is not unexpected, due to the dimeric nature of both AXL-Fc and tilvestamab. Based on these data, we decided to move further with smaller fragments of both proteins, i.e. Fab fragments of tilvestamab and monomeric AXL extracellular domain, without the Fc dimerisation domain.

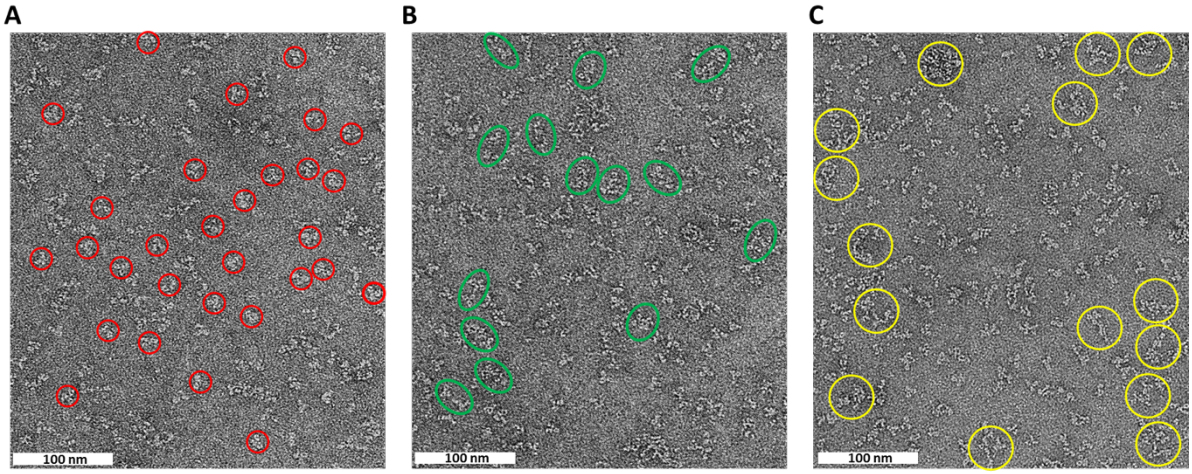

Figure 1. Negative-stain TEM analysis of AXL-Fc and tilvestamab. Representative micrographs of negative-stained molecules showing (**A)** predominantly monomeric tilvestamab particles marked with red circles, (**B)** an increased presence of dimeric tilvestamab particles shown as green ovals, (**C)** larger particles upon mixing tilvestamab with Axl-Fc circled in yellow. Scale bar: 100 nm.

sAXL-tilvestamab solution structures using SAXS

As the next step after characterizing the sAXL-tilvestamab Synchrotron SAXS data were collected in SEC mode for different combinations of AXL-Fc, sAXL, tilvestamab, Fab, and anti-NabFab nanobody. 3D models were built using DAMMIN for all components separately, and MONSA was run with simultaneous input of 5 scattering curves and 3 protein phases (sAXL, Fab, Nb). SAXS parameters are shown in Table 1 and results in **Fig. 2-3**.

226 The AXL-Fc fusion was shown to be a very elongated, flexible dimer by SAXS, and
227 mixing it with the full tilvestamab antibody resulted in large, heterogeneous complexes
228 that could not be fully resolved even in SEC-SAXS (unpublished data, **Fig. 2**); these
229 results agree with the negative stain EM results above. Therefore, the Fab fragment
230 of tilvestamab was purified and used for additional SAXS experiments, to decrease
231 sample heterogeneity.

232 AXL-Fc mixed with the Fab resulted in a heterotetrameric 2:2 complex, as expected
233 (**Fig. 2**). This complex was even more elongated than the AXL-Fc dimer, indicating
234 that the Fab bound close to the N terminus of AXL (the Fc fusion is C-terminal). For
235 further analyses, the Fc fragment was cleaved from the fusion, and the monomeric,
236 soluble AXL extracellular domain (sAXL) was analysed alone and with tilvestamab.

237 sAXL alone was elongated, as previously seen[25], having the four folded domains like
238 beads on a string, similarly to the AlphaFold model. The Fab fragment increased the
239 length and volume of the particle, and the MW corresponded to that of the expected
240 1:1 heterodimer (**Fig. 3**). Additionally, the anti-Fab nanobody was used to build a
241 ternary complex, and the result indicated a further small increase in both R_g, D_{max}, and
242 the molecular weight, showing that a 1:1:1 complex had been formed. The low-
243 resolution structures from SAXS experiments therefore indicated an elongated,
244 flexible structure for AXL and the binding of the antibody to the first Ig domain of AXL,
245 as expected.

246

247 **Table 1. SAXS parameters.** All data were collected using a SEC-SAXS setup. The
248 MW corresponds to the Bayesian estimate given by PRIMUS. R_g comes from the
249 Guinier plot in PRIMUS and D_{max} from the distance distribution analysis in GNOM. *Ab*
250 *initio* model volumes from DAMMIN are also shown, and they are affected by both
251 MW, particle shape, and flexibility.

sample	R_g (Å)	D_{max} (Å)	MW (kDa)	DAMMIN model volume (nm^3)
AXL-Fc	76.1	300	242	491
tilvestamab	51.5	200	147	329
AXL-Fc + tilvestamab	155.2	600	790	3537
AXL-Fc + Fab	101.4	400	318	754
sAXL	48.8	180	60	136

sAXL + Fab	62.2	267	114	242
Fab	26.1	85	48	64
sAXL + Fab + Nb	63.7	280	119	262
Fab + Nb	27.6	85	64	87

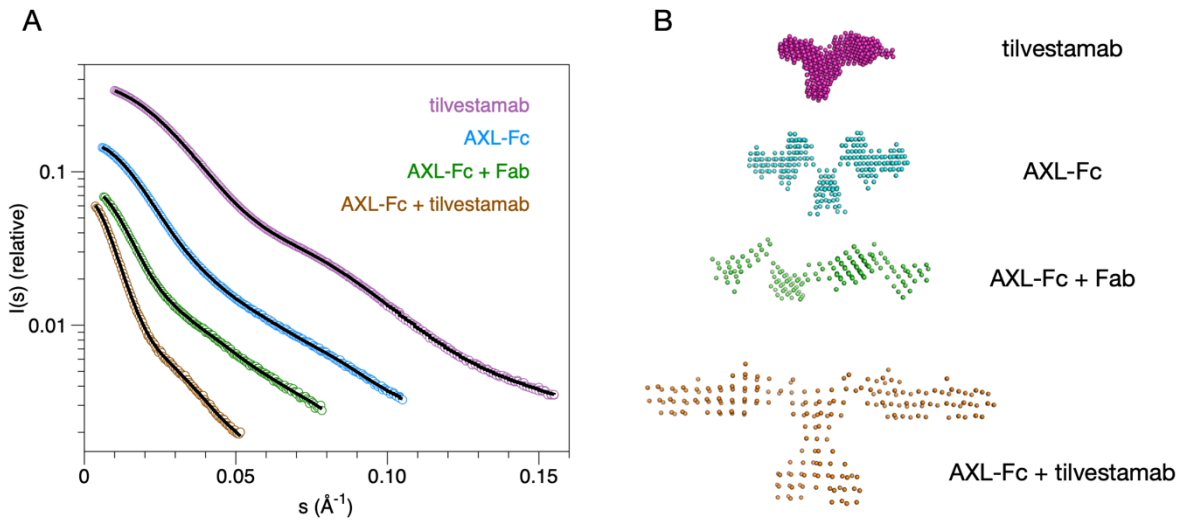

Figure 2. SAXS analysis of AXL-Fc and tilvestamab. (**A**) Scattering curves and DAMMIN model fits. (**B**) Dummy atom-based SAXS models of full-length AXL-Fc and tilvestamab.

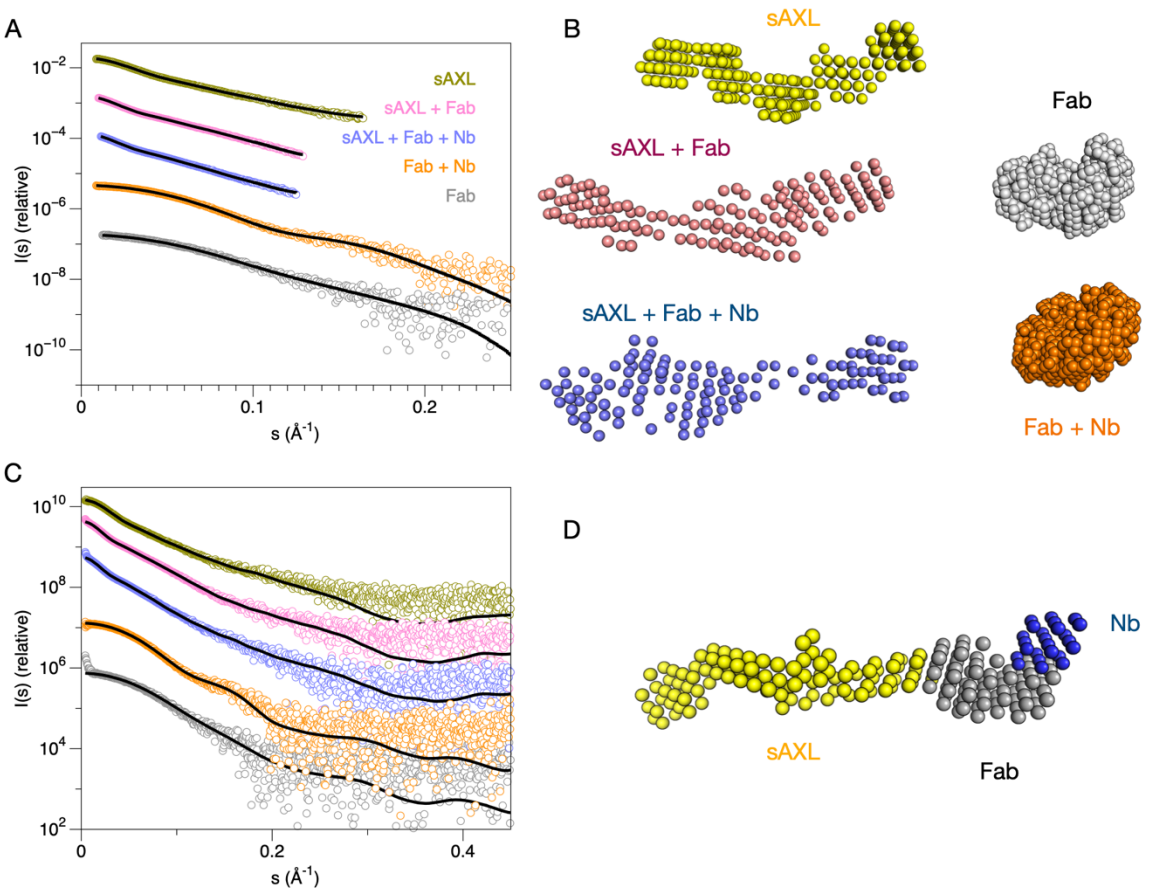

Figure 3. SAXS analysis for truncated variants. (A) Scattering curves and DAMMIN fits. (**B)** Dummy atom-based SAXS models for different combinations of sAXL, tilvestamab Fab, and anti-NabFab nanobody. (**C)** Fits to the same curves as in **A**, during multi-phase simultaneous fitting in MONSA. (**D)** A multi-phase model of the complex is shown, resulting from the simultaneous fitting of 5 different SAXS curves and 3 protein phases (sAXL, Fab, Nb).

Cryo-EM study for the AXL-tilvestamab Fab complex

Initial cryo-EM studies on AXL-Fc complexed with the tilvestamab Fab showed high degrees of flexibility of a very elongated, heterogeneous complex (unpublished data), in line with the SAXS data above. Therefore, monomeric sAXL was complexed with the tilvestamab Fab bound to anti-Fab nanobody for cryo-EM.

To obtain a higher-resolution insight into the complex between AXL and tilvestamab, especially the epitope-paratope interactions, we prepared samples for cryo-EM experiments and collected data from a sample of monomeric sAXL, the tilvestamab Fab, and the anti-Fab nanobody. We expected sAXL to be flexible even within this ternary complex, based on the SAXS data from the components and complexes (**Fig. 3**). In line with this, density was observed for the first Ig1 domain of AXL, while the tilvestamab Fab domain and the anti-Fab nanobody were clearly defined.

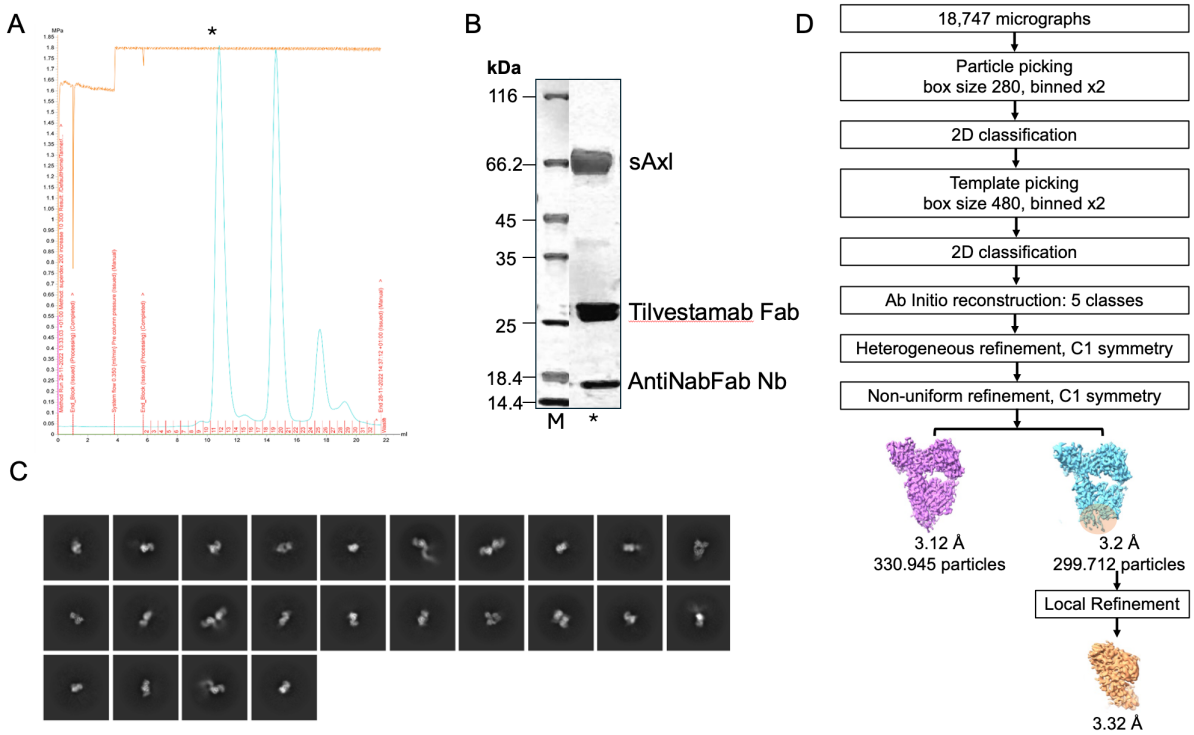

Figure 4. Cryo-EM sample preparation and processing. (A) Size exclusion profiles of Fab, Axl-Fc, and the anti-NabFab Nanobody (Nb). **(B)** SDS-PAGE of the peak complex fraction (*) was used for sample preparation for cryo-EM. **(C)** 2D classes, and **(D)** Schematic representation of the processing workflow.

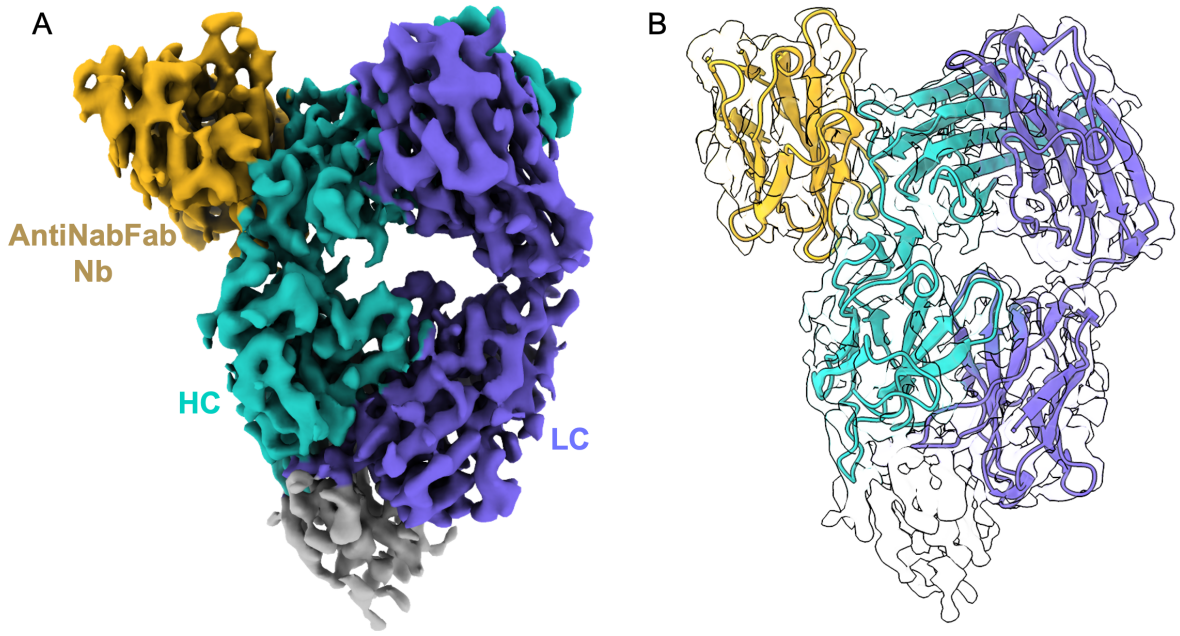

Figure 5. Reconstruction of the tilvestamab Fab-Nb complex. (A) Final refined 3D map at 3.12 Å resolution. Density for HC is shown in turquoise, purple for LC, and orange for the anti-NabFab nanobody. **(B)** Refined atomic model fitted into the map.

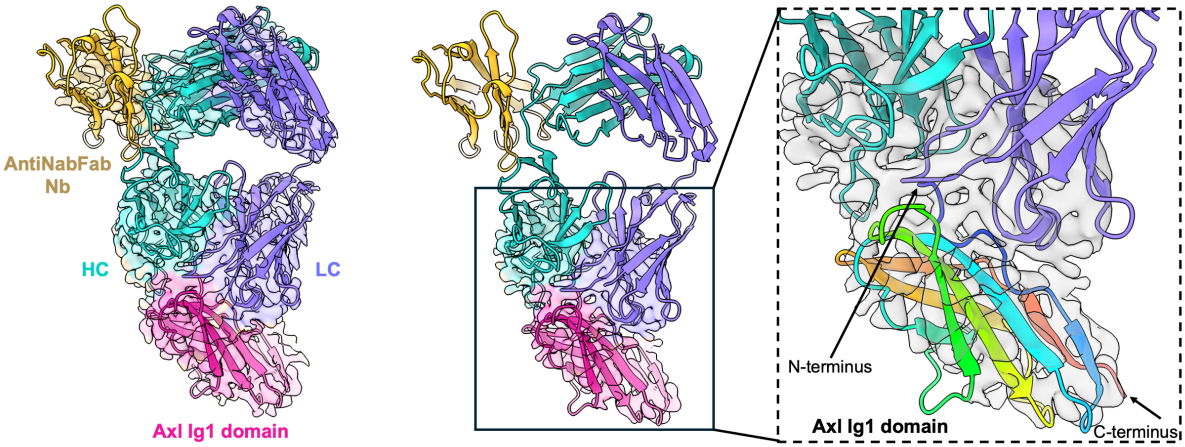

Figure 6. Fitting of the AXL Ig1 domain after local map refinement. The local refinement clearly establishes the orientation of the antigen AXL Ig1 domain with respect to the antibody.

Table 2. Data collection and refinement statistics.

Data collection	
Magnification	130 000 x
Defocus range (mm) -Voltage (kV)	-300
Microscope	Titan Krios
Detector	Falcon 3
No. of frames	53
Pixel size (Å/pixel)	0.647
Electron dose (e^-/Å^2)	59.6
No. of micrographs	18747
Reconstruction (CryoSPARC)	
No. of particles	330945
Box size (px)	480
Average resolution (Å) (FSC=0.143)	3.12
Model resolution (Å) (FSC=0.5)	-
Map sharpening B-factor (Å^2)	-
Model building (Phenix 1.21.1_5286)	
No. of chains	3
No. of atoms	4219
No. of amino acid residues	552
No. of ligand atoms	0

Average B-factor (Å^2)	48.94
R.m.s.d. bond lengths (Å)	0.004
R.m.s.d. bond angles (°)	0.598
CC volume	0.79
CC masked	0.82
Molprobity score	1.85
Clash score	11.1
Ramachandran plot favored/allowed/outliers (%)	95.79/4.21/0
Rama-Z (whole/helix/sheet/loop)	0.37/1.24/0.34/0.39
Deposition codes	
PDB	-
EMDB	-

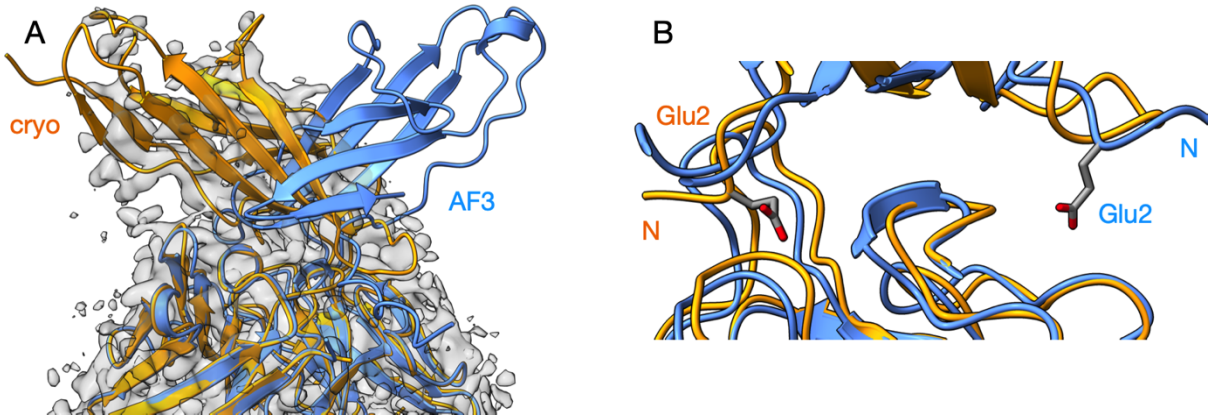

Figure 7. Cryo-EM model vs. AlphaFold3 prediction. (**A**) Comparison of the cryo-EM map and the AlphaFold3 model. Orange is the experimental fit (same as in **Fig. 6** after local refinement) to the cryo-EM map (gray, as in **Fig. 5**), and blue shows the superimposed AlphaFold3 model. The Ig1 domain of AXL, pointing to the right, has a different orientation, linked by a 180° rotation, between the experimental and predicted structures, showing prediction of the binding surfaces, but false orientation. (**B**) In both the experimental and predicted models, Glu2 of AXL Ig1 is directly involved in the interaction, suggesting that AlphaFold3 has identified the interacting surfaces but missed the correct orientation of AXL Ig1.

Comparison of the cryoEM map to the AlphaFold3 model shows that while the Fab-Nb complex is well in place and the binding interfaces on both AXL Ig1 and tilvestamab are correctly identified by the prediction, the orientation of the AXL Ig1 domain is flipped by approximately 180° between the experimental map and the model. This indicates that, as already known for antigen-antibody complexes[24,39], AI-based methods may sometimes fare poorly in predictions of antibody-antigen interactions,

308 and experimental methods still are crucial for deciphering the exact binding mode
309 between the paratope and epitope.

310 As tilvestamab was characterised to block signalling along the GAS6-AXL axis, we
311 compared the cryo-EM model to the crystal structure of AXL Ig1-2 with GAS6[12]. It
312 becomes evident that the binding sites for GAS6 and tilvestamab are next to each
313 other, with a small overlap (**Fig. 8**). This can explain, why tilvestamab does not fully
314 block GAS6 binding[22], while it fully inhibits downstream signalling[20,22,23]. The effect is
315 likely a combination of weakening of GAS6-AXL interactions, conformational changes,
316 and prevention of the formation of functional GAS6-AXL receptor complexes with
317 correct AXL dimerisation in the context of the full-length proteins. Antibody-mediated
318 prevention of dimerisation was suggested before for pembrolizumab and its target PD-
319 1 receptor[40]. It is important to remember that this analysis is based on cryo-EM and
320 crystal structures of truncated proteins, and conformational aspects of full-length
321 proteins are not captured.

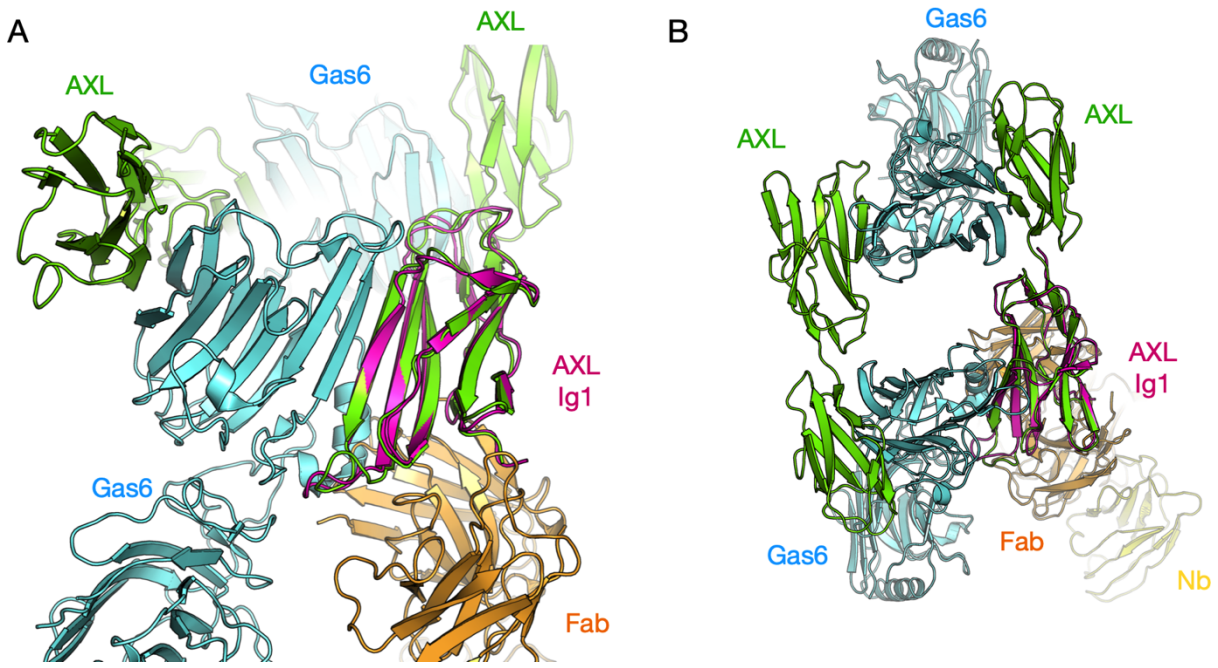

322

323 **Figure 8. Comparison of the cryo-EM model (magenta/orange/yellow) to the GAS6-AXL complex**
324 **crystal structure (green/cyan). (A)** A view from the side of the AXL-GAS6 heterotetramer. The
325 tilvestamab Fab binding overlaps slightly with the GAS6 binding site on AXL Ig1. **(B)** The top view of
326 the heterotetramer indicates that tilvestamab binding does not directly interfere with oligomerisation,
327 but its effects could be mediated through conformational changes.

328

329 **Conclusion**

330 We have presented the first experimental results on the 3D structure of the complex
331 between the AXL extracellular domain and tilvestamab. AXL alone had already earlier
332 been shown to be highly extended and flexible, and in line with this, it remains
333 elongated in the presence of tilvestamab and its Fab fragment, supporting the binding
334 of tilvestamab to the first Ig domain of AXL. The structural data, which also highlight
335 the importance of experimental structural data especially for antigen-antibody
336 complexes, will allow further development of tilvestamab and other specific AXL
337 binders for therapeutic and diagnostic applications.
338
339

Acknowledgements

This work was funded by an Industrial PhD grant from the Research Council of Norway (311399). We acknowledge the use of the Core Facility for Biophysics, Structural Biology, and Screening (BiSS) at the University of Bergen, which has received infrastructure funding from the Research Council of Norway through NORCRYST (grant number 245828) and NOR–OPENSCREEN (grant number 245922). This work has been supported by iNEXT-Discovery, grant number 871037, funded by the Horizon 2020 program of the European Commission. Access to iNano cryo-EM facilities at Aarhus University was thereby supported by iNext-Discovery project numbers 12416, 20077, and 25639. We thank Remy Loris (VIB-VUB Center for Structural Biology & Vrije Universiteit Brussel) for providing access to JEM-1400 electron microscope. We further acknowledge provision of synchrotron beamtime and excellent on-site support for SAXS experiments at Soleil synchrotron and MAX-IV.

Declaration of Interests

JBL and DM are founders and shareholders of BerGenBio ASA. DM is current and JBL and EC are former employees of BerGenBio ASA. The studies were financed by BerGenBio ASA and the Research Council of Norway (Grant Number 311399). The remaining authors declare no conflict of interest.

References

1 Lemke, G. & Rothlin, C. V. Immunobiology of the TAM receptors. *Nat Rev Immunol* **8**, 327-336 (2008). https://doi.org:10.1038/nri2303

2 Miao, Y. R., Rankin, E. B. & Giaccia, A. J. Therapeutic targeting of the functionally elusive TAM receptor family. *Nat Rev Drug Discov* **23**, 201-217 (2024). https://doi.org:10.1038/s41573-023-00846-8

3 DeRyckere, D., Huelse, J. M., Earp, H. S. & Graham, D. K. TAM family kinases as therapeutic targets at the interface of cancer and immunity. *Nat Rev Clin Oncol* **20**, 755-779 (2023). https://doi.org:10.1038/s41571-023-00813-7

4 Goyette, M. A. & Cote, J. F. AXL Receptor Tyrosine Kinase as a Promising Therapeutic Target Directing Multiple Aspects of Cancer Progression and Metastasis. *Cancers (Basel)* **14** (2022). https://doi.org:10.3390/cancers14030466

5 Bellan, M. *et al.* Gas6/TAM System: A Key Modulator of the Interplay between Inflammation and Fibrosis. *Int J Mol Sci* **20** (2019). https://doi.org:10.3390/ijms20205070

6 Wang, Z. Y., Wang, P. G. & An, J. The Multifaceted Roles of TAM Receptors during Viral Infection. *Virol Sin* **36**, 1-12 (2021). https://doi.org:10.1007/s12250-020-00264-9

7 O'Bryan, J. P. *et al.* axl, a transforming gene isolated from primary human myeloid leukemia cells, encodes a novel receptor tyrosine kinase. *Mol Cell Biol* **11**, 5016-5031 (1991). https://doi.org:10.1128/mcb.11.10.5016-5031.1991

8 Varnum, B. C. *et al.* Axl receptor tyrosine kinase stimulated by the vitamin K-dependent protein encoded by growth-arrest-specific gene 6. *Nature* **373**, 623-626 (1995). https://doi.org:10.1038/373623a0

9 Mark, M. R., Chen, J., Hammonds, R. G., Sadick, M. & Godowsk, P. J. Characterization of Gas6, a member of the superfamily of G domain-containing proteins, as a ligand for Rse and Axl. *J Biol Chem* **271**, 9785-9789 (1996). https://doi.org:10.1074/jbc.271.16.9785

10 Nagata, K. *et al.* Identification of the product of growth arrest-specific gene 6 as a common ligand for Axl, Sky, and Mer receptor tyrosine kinases. *J Biol Chem* **271**, 30022-30027 (1996). https://doi.org:10.1074/jbc.271.47.30022

11 Engelsen, A. S. T. *et al.* Dissecting the Role of AXL in Cancer Immune Escape and Resistance to Immune Checkpoint Inhibition. *Front Immunol* **13**, 869676 (2022). https://doi.org:10.3389/fimmu.2022.869676

12 Sasaki, T. *et al.* Structural basis for Gas6-Axl signalling. *EMBO J* **25**, 80-87 (2006). https://doi.org:10.1038/sj.emboj.7600912

13 Pidkovka, N. & Belkhiri, A. Altered expression of AXL receptor tyrosine kinase in gastrointestinal cancers: a promising therapeutic target. *Front Oncol* **13**, 1079041 (2023). https://doi.org:10.3389/fonc.2023.1079041

14 Gay, C. M., Balaji, K. & Byers, L. A. Giving AXL the axe: targeting AXL in human malignancy. *Br J Cancer* **116**, 415-423 (2017). https://doi.org:10.1038/bjc.2016.428

15 Corno, C. *et al.* Role of the Receptor Tyrosine Kinase Axl and its Targeting in Cancer Cells. *Curr Med Chem* **23**, 1496-1512 (2016). https://doi.org:10.2174/0929867323666160405112954

16 Wu, X. *et al.* AXL kinase as a novel target for cancer therapy. *Oncotarget* **5**, 9546-9563 (2014). https://doi.org:10.18632/oncotarget.2542

17 Yu, Y. *et al.* Discovery of A-910, a Highly Potent and Orally Bioavailable Dual MerTK/Axl-Selective Tyrosine Kinase Inhibitor. *J Med Chem* **67**, 17000-17032 (2024). https://doi.org:10.1021/acs.jmedchem.4c01450

18 Ludwig, K. F. *et al.* Small-Molecule Inhibition of Axl Targets Tumor Immune Suppression and Enhances Chemotherapy in Pancreatic Cancer. *Cancer Res* **78**, 246-255 (2018). https://doi.org:10.1158/0008-5472.CAN-17-1973

19 Gajiwala, K. S. *et al.* The Axl kinase domain in complex with a macrocyclic inhibitor offers first structural insights into an active TAM receptor kinase. *J Biol Chem* **292**, 15705-15716 (2017). https://doi.org:10.1074/jbc.M116.771485

20 Chen, T. J. *et al.* AXL targeting by a specific small molecule or monoclonal antibody inhibits renal cell carcinoma progression in an orthotopic mice model. *Physiol Rep* **9**, e15140 (2021). https://doi.org:10.14814/phy2.15140

21 Bohan, D. *et al.* Phosphatidylserine receptors enhance SARS-CoV-2 infection. *PLoS Pathog* **17**, e1009743 (2021). https://doi.org:10.1371/journal.ppat.1009743

22 Bløø, M. *et al.* Tilvestamab, a novel clinical stage humanized anti-AXL function blocking antibody. *Eur J Cancer* **138**, S44 (2020). https://doi.org:https://doi.org/10.1016/S0959-8049(20)31192-8

23 Nilsson, L. H. *et al.* Tilvestamab, a Function-Blocking Monoclonal Antibody Inhibitor of Axl Rtk Signalling, Limits the Onset of Renal Fibrotic Changes in Human Kidneys. *Nephrol Dial Transpl* **36**, 25-25 (2021).

24 Abramson, J. *et al.* Accurate structure prediction of biomolecular interactions with AlphaFold 3. *Nature* **630**, 493-500 (2024). https://doi.org:10.1038/s41586-024-07487-w

25 Tenstad, O. *et al.* In vivo turnover and biodistribution of soluble AXL: implications for biomarker development. *Sci Rep* **14**, 16141 (2024). https://doi.org:10.1038/s41598-024-66665-y

26 Bloch, J. S. *et al.* Development of a universal nanobody-binding Fab module for fiducial-assisted cryo-EM studies of membrane proteins. *Proc Natl Acad Sci U S A* **118** (2021). https://doi.org:10.1073/pnas.2115435118

27 Hammarstrom, M., Woestenenk, E. A., Hellgren, N., Hard, T. & Berglund, H. Effect of N-terminal solubility enhancing fusion proteins on yield of purified target protein. *J Struct Funct Genomics* **7**, 1-14 (2006). https://doi.org:10.1007/s10969-005-9003-7

28 Thureau, A., Roblin, P. & Pérez, J. BioSAXS on the SWING beamline at Synchrotron SOLEIL. *J Appl Crystallogr* **54**, 1698-1710 (2021).

29 Manalastas-Cantos, K. *et al.* ATSAS 3.0: expanded functionality and new tools for small-angle scattering data analysis. *J Appl Crystallogr* **54**, 343-355 (2021). https://doi.org:10.1107/S1600576720013412

30 Panjkovich, A. & Svergun, D. I. CHROMIXS: automatic and interactive analysis of chromatography-coupled small-angle X-ray scattering data. *Bioinformatics (Oxford, England)* **34**, 1944-1946 (2018). https://doi.org:10.1093/bioinformatics/btx846

31 Svergun, D. I. Determination of the regularization parameter in indirect-transform methods using perceptual criteria. *Journal of Applied Crystallography* **25**, 495-503 (1992). https://doi.org:10.1107/S0021889892001663

32 Svergun, D. I. Restoring low resolution structure of biological macromolecules from solution scattering using simulated annealing. *Biophysical journal* **76**, 2879-2886 (1999). https://doi.org:10.1016/S0006-3495(99)77443-6

33 Kahnt, M. *et al.* Measurement of the coherent beam properties at the CoSAXS beamline. *J Synchrotron Radiat* **28**, 1948-1953 (2021). https://doi.org:10.1107/s1600577521009140

34 Punjani, A., Rubinstein, J. L., Fleet, D. J. & Brubaker, M. A. cryoSPARC: algorithms for rapid unsupervised cryo-EM structure determination. *Nat Methods* **14**, 290-296 (2017). https://doi.org:10.1038/nmeth.4169

35 Meng, E. C. *et al.* UCSF ChimeraX: Tools for structure building and analysis. *Protein Sci* **32**, e4792 (2023). https://doi.org:10.1002/pro.4792

36 Emsley, P., Lohkamp, B., Scott, W. G. & Cowtan, K. Features and development of Coot. *Acta Crystallogr D Biol Crystallogr* **66**, 486-501 (2010). https://doi.org:10.1107/S0907444910007493

37 Kidmose, R. T. *et al.* Namdinator - automatic molecular dynamics flexible fitting of structural models into cryo-EM and crystallography experimental maps. *IUCrJ* **6**, 526-531 (2019). https://doi.org:10.1107/S2052252519007619

38 Liebschner, D. *et al.* Macromolecular structure determination using X-rays, neutrons and electrons: recent developments in Phenix. *Acta Crystallogr D Struct Biol* **75**, 861-877 (2019). https://doi.org:10.1107/S2059798319011471

39 Alexander, L. T. *et al.* Protein target highlights in CASP15: Analysis of models by structure providers. *Proteins* **91**, 1571-1599 (2023). https://doi.org:10.1002/prot.26545

40 Horita, S. *et al.* High-resolution crystal structure of the therapeutic antibody pembrolizumab bound to the human PD-1. *Sci Rep* **6**, 35297 (2016). https://doi.org:10.1038/srep35297